

1

2

3 **Main Manuscript for**4 **Strong enhancement of magnetic ordering temperature and**
5 **structural/valence transitions in EuPd₃S₄ under high pressure**

6

7 Shuyuan Huyan^{1,2}, Dominic H. Ryan^{3,*}, Tyler J. Slade^{1,2}, Barbara Lavina^{4,5}, Greeshma Jose⁶,
8 Haozhe Wang⁷, John M. Wilde^{1,2}, Raquel A. Ribeiro^{1,2}, Jiyong Zhao⁵, Weiwei Xie⁷, Wenli Bi⁶,
9 Esen E. Alp⁵, Sergey L. Bud'ko^{1,2,*}, Paul C. Canfield^{1,2,*}

10

11 ¹ *Ames National Laboratory, US DOE, Iowa State University, Ames, Iowa 50011, USA*12 ² *Department of Physics and Astronomy, Iowa State University, Ames, Iowa 50011, USA*13 ³ *Physics Department and Centre for the Physics of Materials, McGill University, 3600 University
14 Street, Montreal, Quebec, H3A 2T8, Canada*15 ⁴ *Center for Advanced Radiation Sources, The University of Chicago, Chicago, IL 60637, USA*16 ⁵ *Advanced Photon Source, Argonne National Laboratory, Argonne, IL 60439, USA*17 ⁶ *Department of Physics, University of Alabama at Birmingham, Birmingham, AL 35294, USA*18 ⁷ *Department of Chemistry, Michigan State University, 578 S Shaw Lane, East Lansing, MI
19 48824, USA*

20 * Dominic H. Ryan

21 **Email:** dominic.ryan@mcgill.ca

22 * Sergey L. Bud'ko

23 **Email:** budko@ameslab.gov

24 * Paul C. Canfield

25 **Email:** canfield@ameslab.gov26 **Author Contributions:** P.C.C., S.L.B., and D.H.R. designed the research. T.J.S., and D.H.R.
27 grew the samples. S.H., D.H.R., B.L., G.J., H.W., R.A.R., J.Z., W.X., W.B., and E.E.A. performed
28 the experiments. S.H., D.H.R., B.L., J.W., W.B., and E.E.A. analyzed the data. S.H., D.H.R.,
29 S.L.B., and P.C.C. wrote the paper. All authors contributed to the discussion of the results and
30 the manuscript.31 **Competing Interest Statement:** The authors declare no competing interests.32 **Classification:** Experimental condensed matter physics, high pressure physics.

33 **Keywords:** Mixed-valency, high pressure effect, antiferromagnetism, structural transition,
34 valence transition.

35 **This PDF file includes:**

36 Main Text

37 Figures 1 to 6

38 **Abstract**

39 We present a comprehensive study of the inhomogeneous mixed valence compound, EuPd_3S_4 ,
40 by electrical transport, x-ray diffraction, time-domain ^{151}Eu synchrotron Mössbauer spectroscopy,
41 and x-ray absorption spectroscopy measurements under high pressure. Electrical transport
42 measurements show that the antiferromagnetic ordering temperature, T_N , increases rapidly from
43 2.8 K at ambient pressure to 23.5 K at \sim 19 GPa and plateaus between \sim 19 and \sim 29 GPa after
44 which no anomaly associated with T_N is detected. A pressure-induced first order structural
45 transition from cubic to tetragonal is observed, with a rather broad coexistence region (\sim 20 GPa
46 to \sim 30 GPa) that corresponds to the T_N plateau. Mössbauer spectroscopy measurements show a
47 clear valence transition from approximately 50: 50 Eu^{2+} : Eu^{3+} to fully Eu^{3+} at \sim 28 GPa, consistent
48 with the vanishing of the magnetic order at the same pressure. X-ray absorption data show a
49 transition to a fully trivalent state at a similar pressure. Our results show that pressure first greatly
50 enhances T_N , most likely via enhanced hybridization between the Eu 4f states and the conduction
51 band, and then, second, causes a structural phase transition that coincides with the conversion of
52 the europium to a fully trivalent state.

53 **Significance Statement**

54 The complexities of Ce- and Yb- based systems have been explored extensively and continue to
55 attract attention. By contrast, the rich phenomenology of Eu-based systems remains largely
56 understudied, despite the same potential for coupled valence, volume, electronic and magnetic
57 contributions. As we show here, the inhomogeneous mixed valence EuPd_3S_4 under hydrostatic
58 pressure exhibits an eight-fold increase of the Néel temperature followed by a structural transition
59 to a lower symmetry structure that coincides with a transition to a fully non-magnetic state. Our
60 derived phase diagram differs significantly from the proposed global phase diagram for Eu-
61 compounds further emphasizing both the need for broader study, and the opportunities Eu-based
62 compounds present for developing new insights into, and examples of, mixed valent behavior.

63 **Main Text**

64 **Introduction**

65 In general, mixed valency in f -electron systems occurs when the more-localized f -orbitals of rare-
66 earth elements hybridize with s , p , and/or d electrons. In the presence of a small energy
67 difference between competing valence states (even smaller than f -electron bandwidth), the
68 system can fluctuate among these nearly degenerate states with different degrees of orbital
69 valences. This phenomenon is commonly referred to as a fluctuating valence state [1]. The onset
70 of mixed valence behavior under external pressure, chemical substitutions, or thermal contraction
71 has dramatic consequences on the macroscopic properties of f -electron systems including lattice
72 collapse [2], quenched magnetism [3], superconductivity [4,5], Kondo behavior [6], and quantum
73 criticality [4,5]. Despite being central to f -electron physics, the underlying mechanism of mixed-
74 valence phenomena is still not fully understood due both to experimental limitations and to the
75 lack of an adequate diversity of ideal materials.

76 That said, the inhomogeneous mixed valence behavior of europium in EuPd_3S_4 is rather special
77 and offers the opportunity to study Eu mixed valency in a novel limit. The rare-earth palladium

78 bronzes, RPd_3S_4 , were reported to crystallize in the cubic NaPt_3O_4 structure ($Pm\bar{3}n$, space group
79 (SG) #223) with the rare earth occupying the $2a$ site and forming a bcc sublattice [7]. Whereas
80 the RPd_3S_4 compounds exist for all the trivalent rare earths, they do not appear to form with the
81 divalent alkaline earths (Ca, Sr,...). Interestingly, when prepared with europium [7] or ytterbium
82 [8] a roughly 50:50 mix of divalent and trivalent rare earth was found, which makes the
83 intermediate valence in these two compounds distinct from the more general fluctuating valence
84 phenomenon case. In EuPd_3S_4 , 50 % Eu^{2+} makes the material magnetic as observed in
85 Mössbauer spectroscopy and thermodynamic measurements [7,9]. By chemical substitution,
86 smaller Y^{3+} ions tend to replace Eu^{3+} sites first and make the valence of Eu more divalent;
87 however, substitution with bigger La^{3+} ions on the other hand, promotes the electron hopping
88 between Eu^{2+} and Eu^{3+} , leading to an intermediate Eu valence until 60% of Eu have been
89 replaced, above which, Eu becomes more trivalent. The chemical substitution work suggests that
90 preservation of the unit cell volume size is a dominant factor controlling the Eu^{2+} : Eu^{3+} valence
91 ratio [9]. Very recently, it was found that rather than adopting the $Pm\bar{3}n$ structure with a single,
92 crystallographic Eu site ($2a$) hosting the two Eu valences, EuPd_3S_4 was found to take the more
93 reasonable cubic $Pm\bar{3}$ (SG #200) structure with two distinct Eu sites ($1a$ and $1b$) below 340 K at
94 ambient pressure [10]. As such then, EuPd_3S_4 allows for the study of valence changes in an
95 inhomogeneously mixed valence system.

96 Considering that chemical substitution and the associated changes in unit cell were shown to
97 profoundly impact the mixed valence state in EuPd_3S_4 , it is worthwhile to appreciate that the
98 effect of external pressure has proven to be an effective way to tune the atomic distances and
99 thus may be used to increase the degree of orbital hybridization, and is considered to be a
100 cleaner and more powerful tool for modifying the valence state than chemical doping. Here, we
101 report the systematic high-pressure investigation of EuPd_3S_4 using a combined experimental
102 approach including electrical transport measurements, x-ray diffraction (XRD), time-domain
103 synchrotron Mössbauer spectroscopy (SMS) [11], and partial fluorescence-yield x-ray absorption
104 spectroscopy (PFY-XAS). A significant, about 8-fold, enhancement in antiferromagnetic transition
105 temperature, (T_N) from ~ 2.8 K at ambient pressure [7] to ~ 3.5 K at ~ 19 GPa is observed.
106 Subsequently, in a pressure window from ~ 19 GPa to ~ 29 GPa, T_N is almost pressure
107 independent, whereas the size of the resistance drop below T_N is gradually suppressed with
108 increasing pressure. The sample in this pressure window is found to be in a mixed phase of cubic
109 and tetragonal structures with the ratio of cubic/tetragonal decreasing with increasing pressure.
110 Above ~ 29 GPa, an abrupt disappearance of antiferromagnetic (AFM) order is observed. In the
111 same pressure range, both SMS and XAS measurements show a clear change from 50: 50 Eu^{2+} :
112 Eu^{3+} to fully Eu^{3+} and is coincident with the complete disappearance of the lower pressure, cubic
113 phase, resulting in a single phase of the non-moment bearing tetragonal structure. This
114 comprehensive study beautifully illustrates the interplay of crystal structure, magnetic ground
115 state, and the associated valence state tuned by high pressure, and suggests that EuPd_3S_4
116 provides a clean and simple system for the detailed study of how magnetism, valence and
117 structure are intertwined and should serve as a benchmark for theoretical efforts to model and
118 understand mixed-valence behavior.

119 **Results**

120 Fig. 1(a) presents the temperature dependence of the resistance, $R(T)$, of single crystalline
121 EuPd_3S_4 under pressure up to ~ 32 GPa. The overall $R(T)$ behavior is metallic over the whole
122 temperature and pressure ranges covered here. A clear resistance drop is seen below 2.8 K at
123 0.4 GPa, reflecting the loss of spin disorder scattering as antiferromagnetic (AFM) ordering
124 occurs. We define the Néel temperature, T_N , as the mid-point of the step in the temperature
125 derivative of resistance (dR/dT), with the uncertainty taken as half of the step width, as shown in
126 Fig. 1(b). T_N at 0.4 GPa is consistent with the ambient pressure heat capacity and magnetization
127 results reported previously [7,9]. Increasing the pressure from 0.4 GPa to ~ 19 GPa leads to a
128 marked rise in T_N from 2.8 K to 23.5 K, Fig. 1(d). Above 20 GPa, there is a sharp increase in
129 resistance; the position of the T_N step remains essentially unchanged, but the size of the step-like

130 feature in dR / dT becomes progressively smaller and is lost by ~ 29 GPa (Fig. 1(b)). As will be
131 shown below, when we examine the powder x-ray data, these changes are consistent with the
132 observation that for ~ 19 - 29 GPa, the system passes through a crystallographic two-phase
133 region as the increasing pressure progressively converts the AFM-ordering Eu^{2+} -containing phase
134 into a fully trivalent non-magnetic phase. Above ~ 29 GPa, the features marking loss of spin-
135 disorder scattering in the resistance, associated with the step like feature in dR / dT are gone, and
136 no further evidence for magnetic ordering (at least above 1.8 K, our lowest measurement
137 temperature) is observed, suggesting that the conversion is now complete. In addition to the step
138 like feature that is related to T_N , a slope change in dR / dT at lower temperature (marked as T^* , in
139 Fig. 1(b)) is also observable at and above 12 GPa and becomes clearer as pressure increases to
140 ~ 19 GPa (Fig. 1(b)). Similar features in dR / dT are common in rare earth bearing compounds and
141 are often associated with incommensurate-to-commensurate transitions or spin re-orientations
142 [12,13]. Of note is that the shape of the higher temperature $R(T)$ curve clearly changes from
143 concave-like at low pressures to convex-like at high pressures, indicating possible change of
144 band structure and/or paramagnetic and phonon scattering.

145 The Néel temperature, T_N , and anomaly, T^* , as functions of the pressure for EuPd_3S_4 are
146 presented in Fig. 1(d). We can see that with increasing pressure, T_N has an approximately eight-
147 fold enhancement from 2.8 K at 0.4 GPa to around 23.5 K at ~ 19 GPa with an average increasing
148 rate of ~ 1.1 K/GPa, then T_N remains essentially constant from ~ 19 GPa to ~ 29 GPa, above which
149 signatures of antiferromagnetic ordering are not observed. Meanwhile, resistance versus
150 pressure (Fig. 1(c)) at all temperatures shows an abrupt increase starting from ~ 22 GPa. This is
151 most likely due to the onset of a crystallographic two-phase region (as will be discussed below)
152 but may also be associated with the commensurate change in valence and therefore band
153 structure. As will be discussed further below, the flat T_N versus P region between ~ 19 GPa and
154 ~ 29 GPa is most likely the result of entering a region of mixed crystallographic phases with
155 increasing pressure leading to a larger fraction of the smaller volume, purely Eu^{3+} phase. As a
156 result of this two-phase nature, we speculate that the strain on the remaining Eu^{2+} phase remains
157 effectively constant over this pressure range, leading to an effectively constant T_N value.
158 Remarkably, T^* exhibits very similar behavior, rising with T_N and then becoming constant through
159 the two-phase region, reinforcing the idea that in the two-phase region there is relatively little
160 change in strain on the Eu^{2+} fraction of the sample.

161 It is notable that the residual resistance ratio ($RRR = R(300\text{ K}) / R(1.8\text{ K})$) as a function of the
162 pressure shows a different behavior compared with the resistance as a function of the pressure,
163 as shown in Fig. 1(c). The RRR first increases from ~ 40 at 0.4 GPa to ~ 100 at ~ 10 GPa and then
164 rapidly decreases to less than 2 at ~ 22 GPa, above which the resistance at all temperatures
165 shows a sharp increase with the pressure, which might indicate a structural transition. Fig. 1(c)
166 also presents the pressure dependent resistance of the sample at representative temperatures
167 ranging from 1.8 K to 300 K. Each data set shows a marked increase in resistance at ~ 24 GPa
168 indicating that in the temperature range we measured, if there is any structural/valence transition
169 under pressure, the transition temperature should be above 300 K and its phase line is (almost)
170 vertical in temperature-pressure (T - P) plot.

171 To explicitly explore the structural stability of EuPd_3S_4 under pressure, synchrotron powder x-ray
172 diffraction (PXRD) experiments were performed on a sintered powder (polycrystalline) sample up
173 to ~ 57 GPa. Figs. 2(a-c) demonstrates the outcomes. Peaks from copper (calibrant) and rhenium
174 (gasket) are indexed in Figs. 2(b) and 2(c) and are marked with pink stars and blue crosses,
175 respectively, in Fig. S1 to illustrate their systematic shift with pressure. Three distinct pressure
176 regions were detected, as shown in Fig. 2(a): zone I (ambient to ~ 17 GPa), zone II (~ 20 GPa to
177 ~ 32 GPa), and zone III (~ 34 GPa to ~ 57 GPa), respectively. The diffraction patterns in zone I can
178 be indexed to the cubic space group $Pm\bar{3}$ (SG #200), as shown in Fig. 2(b), which is consistent
179 with the structure of the specimen at ambient pressure [10]. In zone III, the patterns are
180 resolvably different and could be assigned to a tetragonal space group, $P4 / mmm$ (SG #123), as
181 depicted in Fig. 2(c). The pressure dependencies of the lattice parameters and unit cell volume
182 EuPd_3S_4 are shown in Figs. 2(d) and 2(e). Clear discontinuous changes in both lattice parameters

183 (a and c) and the unit cell volume (V) are observed. Considering that $P4 / mmm$ (SG #123) is not
184 a translationengleiche subgroup of $Pm\bar{3}$ (SG #200), which is actually a translationengleiche
185 subgroup of $Pm\bar{3}n$ (SG #223), we expect that the structural transition under pressure to be first
186 order according to Hermann's theory [14,15]. The pressure-volume, $P(V)$ curve in zone I was
187 analyzed using a second-order Birch-Murnaghan equation of state (BM EOS) as shown in Fig.
188 2(e). For pressures up to \sim 18 GPa (zone I), the elastic parameters yield a zero-pressure bulk
189 modulus B_0 of 103.5(2.0) GPa and a zero-pressure unit-cell volume V_0 of 297.89 \AA^3 at ambient
190 conditions which is consistent with the reported value [9]. The unit cell volume in zone III shows a
191 clear deviation from the fitted curve based on the data points in zone I with the unit cell volume at
192 \sim 34 GPa decreasing by \sim 4.8%, which is intricately linked to the structural transition and the
193 substantial change in the valence of Eu ions. It is worth mentioning that the fitted parameters in
194 zone I were also obtained from a larger volume of data taken from multiple experimental runs, as
195 shown in Fig. S5.

196 As diffraction peaks from both the cubic and tetragonal phases are observed in zone II, a two-
197 phase scenario is a reasonable interpretation. The gradual disappearance of the cubic phase and
198 the appearance and growth of the tetragonal phase can be seen clearly despite the increasing
199 difficulty of indexing the diffraction patterns within zone II. Fig. 3 shows the changes of the
200 specific diffraction peaks in detail, highlighting the disappearance of the cubic (210) and (211)
201 Bragg peaks and the sudden emergence of the tetragonal (113) peak at \sim 20 GPa. Figs. S2-S4
202 show more detail.

203 A first-order structural phase transition typically involves a sudden change in lattice parameters
204 and unit cell volume, and the presence of a two-phase region in the intermediate pressure zone.
205 Fig. 2(d) and 2(e) illustrate all these features clearly. However, the large two-phase window, more
206 than 10 GPa, cannot simply be attributed to pressure gradients within the pressure transmitting
207 medium since the pressure gradient in neon at 20 GPa is only 0.15 GPa [16], which is almost two
208 orders of magnitude smaller than the observed two-phase pressure range. The broad two-phase
209 region must therefore be considered to be an intrinsic feature associated with the valence change
210 in EuPd_3S_4 under these conditions. An analogous large two-phase pressure range has also been
211 reported in SmSe, SmTe [17], and CaFe_2As_2 [18,19], possibly as a result of anharmonic strain
212 effects caused by the significant volume mismatch between the various phases [20]. Noteworthy,
213 the Néel temperature plateau in Fig. 1 (d), where T_N (and T^*) are almost independent of pressure,
214 coincides well with the two-phase pressure region that has a mixed phase with shifting phase
215 ratio. In other words, the behavior of the T_N plateau and the gradual loss of magnetic moment in
216 the T_N plateau region are likewise intrinsic and may be closely related to the gradual increase in
217 the relative amount of the tetragonal phase, and as will be shown below, non-magnetic- Eu^{3+} .

218 The conventional, energy-domain, ^{151}Eu Mössbauer spectrum of EuPd_3S_4 shows two, roughly
219 equal-area, well-separated lines from the Eu^{2+} and Eu^{3+} present [7,9]. These two lines reflect the
220 two different transition energies (i.e., isomer shifts), and hence photon frequencies, associated
221 with the two europium valence states. In the time-domain synchrotron Mössbauer spectroscopy
222 (SMS) [11] spectra we observe a simple beat pattern between these two photon frequencies (see
223 Fig. 4(a) at 0.7 GPa) with the beat frequency set by the fractional difference in photon energies
224 (or frequencies), and the amplitude set largely by the relative populations of the two valence
225 states. A visual inspection of Fig. 4(a) reveals that both change with increasing pressure: the beat
226 frequency decreases, and the amplitude modulation generally becomes less distinct. The
227 evolution in beat frequency indicates that the isomer shift difference between the two components
228 is becoming smaller. Finally, there is an abrupt change in the curves above 27 GPa to a relatively
229 very long beat period (rather than the simple exponential decay that we would associate with a
230 single trivalent line) suggesting that the system is not just a cubic crystallographic phase with
231 pure Eu^{3+} .

232 More intuitive energy-domain spectra generated by CONUSS [21] by fitting the time-domain data
233 are shown in Fig. 4(b). Within the pressure range of 0.7 GPa to 27 GPa, two distinct peaks are

234 observed, representing the isomer shifts of Eu²⁺ and Eu³⁺ at low pressures. For clarity, these two
235 peaks are referred to as the Eu²⁺ and Eu³⁺ peaks, although it should be noted that the oxidation
236 state of the Eu²⁺ peak tends to approach that of Eu³⁺ under pressure. The intensity of the Eu²⁺
237 peak weakens around 27 GPa and vanishes at 29.7 GPa, resulting in the sole presence of the
238 Eu³⁺ peak, thereby indicating a complete transition from an initial nearly 50: 50 Eu²⁺: Eu³⁺ state to
239 a fully Eu³⁺ state. Concurrently, the linewidth of Eu³⁺ peak exhibits a clear broadening at 29.7
240 GPa compared to lower pressures. This can be attributed to the presence of a quadrupole
241 interaction, $\Delta E(Q)$, of 2.16(5) mm/s. This observation is consistent with the structural transition
242 from a cubic to a tetragonal phase, where an electric field gradient develops as a result of the
243 reduced symmetry. However, due to the crowded arrangement of multiple components split by
244 the quadrupole interaction within the line width of ~2.3 mm/s, the absorption spectrum is not
245 resolved. Furthermore, the quadrupole interaction, $\Delta E(Q)$, increases within the pressure range of
246 approximately 28 to 30 GPa, as shown in Fig. S6. This increase can be attributed to the increase
247 of structural anisotropy. The observed enhancement in the quadrupole interaction may
248 correspond to the transition from a two-phase region, characterized by the presence of strain
249 between the two phases, to a fully tetragonal phase. Upon decompression, the absorption peak
250 corresponding to Eu²⁺ recovers at ~25 GPa, indicating the reversibility of the pressure-driven
251 transition.

252 The isomer shift exhibited the same evolution with pressure in a second experimental run on a
253 sintered powder sample (SMS data are shown in Fig. S7) as it did for a single crystal sample.
254 Absolute calibration of the isomer shifts of the two components was achieved by measuring SMS
255 spectra at several pressures after introducing a standard (EuS) with a known isomer shift (-
256 11.496 mm/s) in the beam after the pressure cell (detailed explanation of calibration of absolute
257 values of isomer shifts is shown in Fig. S8, S9). These corrected measurements allowed us to
258 show that most of the isomer shift change is due to the Eu²⁺ line moving to more positive values
259 (Fig. 4(c)) with increasing pressure.

260 The pressure dependence of the area fraction of the Eu²⁺ peak is plotted in Fig. 4(d). There are
261 some differences between the powder and single crystal data in the ~21 - 27 GPa pressure range
262 which are not surprising given their different microstructures and internal strain distributions. The
263 pressure dependence of the mean Eu valence was estimated by assuming that the area of each
264 component in the SMS spectrum was proportional to the number of ions associated with the
265 corresponding valence state. The detailed calculation is shown in Fig. S10, and the result is
266 summarized in Fig. 6(d), shown below.

267 Partial fluorescence-yield x-ray absorption spectroscopy (PFY-XAS) measurements were
268 performed to provide independent confirmation of the valence change. As shown in Fig. 5(a), the
269 absorption peak corresponding to Eu²⁺ gradually weakens as the pressure increases to 14 GPa,
270 then becomes much weaker at ~22 GPa, and remains as a small bump for higher pressures,
271 clearly demonstrating a transition from 50: 50 Eu²⁺: Eu³⁺ to essentially Eu³⁺. The valence
272 transition appears at a somewhat lower pressure in the PFY-XAS measurements than in the SMS
273 results. Such a shift may be associated with non-hydrostaticity due to the lack of a pressure
274 transmitting medium (PTM) in the PFY-XAS measurement. The persistence of a tiny Eu²⁺ peak at
275 higher pressures may be attributed to pressure inhomogeneity. Furthermore, a small, but
276 discernible shift towards slightly lower energy of the absorption peak corresponding to Eu³⁺ is
277 noted at and above ~22 GPa. The possible reasons for this tiny shift in the absorption peak
278 position, aside from experimental factors such as energy resolution and XAS instrument
279 calibration, could be a change in the crystal field, which splits the 4f electronic state into different
280 energy levels. This shift could be closely related to the structural transition that begins to occur
281 between ~20 GPa and ~32 GPa. To fully comprehend the mechanism behind the absorption
282 peak shift, additional research, such as DFT calculation based on the more accurate structure, is
283 required.

284 Modeling the PFY-XAS data using a series of Lorentzian and arctangent functions for each
285 absorption peak, as seen in Fig. 5(b), yields the mean valence of the Eu ion. The average
286 valence is estimated using the following formula:

287

$$v = \frac{2 \times A_{\text{Eu}^{2+}} + 3 \times A_{\text{Eu}^{3+}}}{A_{\text{Eu}^{2+}} + A_{\text{Eu}^{3+}}} \#\#(1)$$

288 where $A_{\text{Eu}^{2+}}$ and $A_{\text{Eu}^{3+}}$ are the areas of absorption peaks for Eu^{2+} and Eu^{3+} , respectively. The
289 estimated mean Eu valence as a function of pressure as measured by SMS and XAS are
290 depicted in Fig. 6(d) and (Fig. 5(c) & Fig. 6(e)), respectively. Both measurements demonstrate a
291 clear valence change from Eu^{2+} to Eu^{3+} . The shift is abrupt and occurs at higher pressure ($> \sim 27$
292 GPa) in the SMS measurements with He as the PTM. Due to the low data density and the fact
293 that the high-pressure XAS measurement is conducted without PTM, it is not possible to
294 determine the width of the valence transition; however, it is clear that the mean valence is very
295 close to 3+ at and above 24 GPa.

296 **Discussion**

297 The pressure dependence of the AFM transition temperature T_N , resistance at 1.8 K, the volume
298 of the unit cell, and the mean valences estimated from SMS and PTM data is presented in Fig. 6.
299 Two vertical lines at ~ 20 and 30 GPa mark the lower and upper boundaries of the two-phase
300 region and are shown crossing all the data sets. Although the use of different PTMs and
301 manometers for different high-pressure measurements made at different temperatures may
302 cause some inconsistency in the critical pressures and possible smearing of the first-order
303 transition, a clear picture still can be obtained: There are three distinct pressure regions
304 associated with (i) the low-pressure cubic phase, (ii) an intermediate pressure two-phase region
305 where both cubic and tetragonal phases are present, and finally (iii) the high-pressure tetragonal
306 phase (see Fig. 6(c)). Two pressures (~ 20 GPa and ~ 30 GPa) separate the changes we see in
307 the T - P phase diagram shown in Fig. 6(a) as well as the R (1.8 K) data shown in Fig. 6(b). Fig.
308 6(a) shows that T_N rises rapidly in the low-pressure region, is essentially constant in the
309 intermediate pressure region, and is not detectable (due to the loss of moment bearing Eu^{2+}) in
310 the high-pressure region. Fig. 6(b) shows that the 1.8 K resistance of the low-pressure phase is
311 relatively low and essentially unchanging in the low-pressure phase. In the intermediate pressure
312 region, R (1.8 K) rises substantially in a near linear manner before appearing to saturate above 30
313 GPa. The unit cell volumes for the low-pressure and high-pressure phases are shown in Fig. 6(c).
314 In the two-phase region, there is an increasing amount of tetragonal phase as pressure
315 increases. The estimated mean valence derived from SMS results is shown in Fig. 6(d). The
316 mean valence is nearly constant up to ~ 20 GPa, increases in a non-monotonic manner,
317 depending upon the run and sample, over the next 10 GPa and is fully trivalent at and above 30
318 GPa. The mean valence derived from XAS data in Fig. 6(e) is fully consistent with the SMS data
319 but suffers from two problems. First, the XAS data is the only data set collected without pressure
320 medium, and as such represents very different pressure conditions; second, the XAS data set is
321 too sparse to accurately detect an onset to valence change. All of this said, the XAS data set is
322 qualitatively similar to the SMS data, showing a change from roughly 50: 50 Eu^{2+} : Eu^{3+} to
323 essentially Eu^{3+} by ~ 25 GPa. The fact that this pressure is lower than any seen in the other
324 measurements is most likely associated with the less hydrostatic conditions. Taken all together,
325 then, our diverse data sets are consistent with EuPd_3S_4 being in the low-pressure cubic phase up
326 to ~ 20 GPa. In this pressure range there is a large increase in T_N that we associated with an
327 increasing coupling (or hybridization) between the Eu 4f shell and the conduction electrons.
328 Whereas such large dT_N/dP values are rather uncommon for rare earth compounds, similarly
329 large values have been found for some Eu-based intermetallics, such as EnIn_2As_2 [22], EuSn_2As_2
330 [23], EuSn_2P_2 . [24], and EuMnBi_2 [25].

331 Ultimately, when the coupling (or hybridization) between the conduction electrons and the Eu-4f-
332 shell becomes sufficiently strong, EuPd_3S_4 starts transforming into the high pressure, Eu^{3+} -
333 tetragonal phase and enters the two-phase region of the T - P phase diagram. As more and
334 more of the sample transforms into the smaller volume, tetragonal phase, the residual cubic
335 EuPd_3S_4 remains at a more or less constant strain and constant T_N and T^* . The pressure range
336 of this two-phase region, ~ 20 - 30 GPa, is fully consistent with change in volume of the unit cells
337 (between cubic and tetragonal) and their pressure derivatives (Fig. 2(e)). Finally, near 30 GPa the
338 conversion is complete, and the sample becomes fully tetragonal and fully non-magnetic Eu^{3+} .

339 The EuPd_3S_4 T - P phase diagram differs from the putative "global phase diagram" [26,27] for Eu-
340 based compounds in several ways. Qualitatively the size of the increase in T_N for EuPd_3S_4 is
341 remarkable, over 800% increase by ~ 20 GPa; this is much larger than seen for other Eu-
342 compounds. Quantitatively, the "global phase diagram" has the second order T_N line ending in an
343 isostructural, first order structural phase transition line that has a finite slope and terminates in a
344 critical end point. Whereas, EuPd_3S_4 has a structural phase transition from a low-pressure cubic
345 phase to a high-pressure, trivalent, tetragonal phase with an experimentally vertical phase line
346 and an approximately 10 GPa wide, two phase coexistence region. As such, then, a critical end
347 point is impossible. In this sense, EuPd_3S_4 is a particularly clean, stable, and well-behaved
348 system that even at ambient conditions exhibits a rare, possibly unique, inhomogeneous mixed-
349 valence state, making it a convenient and powerful test bed for models of mixed-valent behavior.
350 In addition, the significant departures from the predicted "global phase diagrams" [26,27] mean

351 that EuPd_3S_4 presents a unique example of pressure induced, valence collapse. Despite the
352 extensive exploration and continued attention given to Ce- and Yb-based systems, the rich
353 phenomenology of Eu-based systems has remained largely uncharted. Our discovery provides a
354 significant prototype within the Eu-based system, revealing distinct behaviors under high
355 pressure, thereby igniting the potential for further in-depth investigations.

356 **Materials and Methods**

357 ***Crystal growth***

358 High quality single crystals of EuPd_3S_4 were grown by a two-step solution growth method by
359 adding Eu to a Pd-S melt [28]. First, a nominal composition of $\text{Eu}_5\text{Pd}_{58}\text{S}_{37}$ was loaded into a fritted
360 alumina crucible set [29,30] and sealed in a fused silica tube. The tube was heated to 1150°C,
361 held for 8 hours, and cooled over 36 hours to 1050°C, after which the liquid was decanted. The
362 tube was opened, all solidified sulfides and oxides were discarded, and the captured decanted
363 liquid reused in a new crucible set. The second crucible set was again sealed and then warmed
364 to 1075°C. After holding for 8 hours, the furnace was slowly cooled over 150 hours to 900°C, at
365 which point the remaining solution was decanted. After cooling to room temperature, the crucibles
366 were opened to reveal large, mirror-faceted crystals [28].

367 The polycrystal samples (used for synchrotron x-ray diffraction, Mössbauer spectroscopy, and x-
368 ray absorption spectroscopy measurements) were prepared by a direct solid-state reaction from a
369 stoichiometric mixture of EuS (99.9%), Pd (99.95%) and S (99.95%) powders [9]. The mixture
370 was pressed into a pellet, loaded in an alumina crucible, and sealed in a fused silica tube with a
371 partial pressure of helium gas. The tube was heated to 650°C over 3 hours, held for an hour and
372 then heated to 900°C over 3 hours, and held for 90 hours before furnace cooling. The resulting,
373 sintered pellets were checked for phase purity by powder x-ray diffraction and then, as needed,
374 ground, repressed into a pellet and heated again to 900°C for further reaction [9].

375 ***High pressure measurements***

376 ***Electrical transport***

377 Linear four-terminal electrical resistivity measurements were performed in a Diamond Anvil cell
378 (DAC) (Bjscistar [31]), with 500 μm culet-size standard cut-type Ia diamonds. EuPd_3S_4 single
379 crystals were cleaved into 20 μm thick flakes and cut and polished into 100 μm x 40 μm plates. A
380 single plate was loaded together with a tiny ruby sphere (< 10 μm in diameter) into an apertured
381 stainless-steel gasket covered by cubic-BN. Platinum foil was used to create electrodes to
382 connect to the sample. Nujol mineral oil was used as pressure transmitting medium (PTM), since:
383 1) this fluid medium can maintain a quasi-hydrostatic pressure environment with a small pressure
384 gradient below its liquid/glass transition [16,32,33]; 2) the use of a fluid medium helps to minimize
385 direct contact between the sample and diamond culet which could lead to an uniaxial pressure
386 component. Pressure was determined by ruby fluorescence [34] at room temperature. Low
387 temperature resistance measurements down to 1.8 K were conducted in the Quantum Design
388 Physical Property Measurement System (PPMS).

389 ***X-ray diffraction (XRD)***

390 Two room-temperature high-pressure powder XRD (PXRD) runs were carried out at the
391 GSECARS 13-BM-D and XSD 3-ID-B Beamlines of the Advanced Photon Source (APS), at
392 Argonne National Laboratory (ANL). X-rays with a wavelength of 0.29521 \AA and 0.4833 \AA were
393 focused to a 15 μm (vertical) x 15 μm (horizontal) spot size at both beamlines. The sintered
394 powder sample and manometer (ruby spheres for runs 1 and 2, Cu powder for run 3) were loaded
395 into a wide opening SSDAC-70 DAC, diamond anvils with 300 μm and 500 μm diameter cullets
396 and Re gaskets were used to contain the sample. Neon was loaded as the PTM. Pressures were
397 determined *in situ* using the ruby scale [34] or the equation of state of the Cu standard (JCPDS

398 04-0836) at the same position where the PXRD data were taken on the sample. The two-
399 dimensional diffraction images were integrated using the DIOPTAS software [35] and Rietveld
400 and Le Bail refinements were performed in GSAS-II [36]. PXRD data shown in main text are all
401 from run 3.

402 ***Synchrotron Mössbauer spectroscopy (SMS)***

403 High-pressure ^{151}Eu SMS [11] experiments were carried out at 3-ID-B Beamline of the APS, at
404 ANL. SMS, also known as nuclear forward scattering (NFS), utilizes a pulsed synchrotron x-ray
405 source to probe nuclear hyperfine interactions in the time domain rather than the energy domain
406 used for conventional Mössbauer spectroscopy. The SMS experiments were performed in the 24-
407 bunch timing mode with a 153 ns separation between successive electron bunches. A specially
408 designed helium-flow cryostat cooled the sample to 50 K while high pressures were generated
409 using a membrane-driven miniature panoramic DAC [37]. 500 μm culet size diamonds were used
410 as anvils and a laser drilled Re gasket formed the sample chamber. The SMS spectra were fitted
411 using the CONUSS software package [21].

412 Both single crystal and sintered powder samples were measured by SMS. All the SMS
413 measurements were performed at 50 K. This temperature was chosen for operational
414 convenience: low enough to benefit from a factor of two increase in the recoil-free fraction (f -
415 factor) compared with ambient temperatures [9] but high enough to remain above the expected
416 pressure-driven increase in T_N . Helium was used as PTM to promote hydrostatic conditions at
417 high pressure. After gas loading at room temperature, all subsequent pressure changes were
418 made by the gas membrane at 50 K. Using an on-line system, laser excited ruby fluorescence
419 spectra were collected for the determination of pressure using the ruby scale [34]. Pressure-
420 induced changes in the europium valence, as well as structure, have been detected through
421 either a change in the isomer shifts of the two pre-existing components (Eu^{2+} and Eu^{3+}) or
422 changes in their relative proportions. Absolute isomer shift values were obtained at several
423 pressures by adding a reference sample (EuS) with a known isomer shift (-11.496 mm/s relative
424 to EuF_3) in the x-ray beam [38-40].

425 ***Partial fluorescence-yield x-ray absorption spectroscopy (PFY-XAS)***

426 PFY-XAS experiments were carried out at the 16ID-D Beamline of the APS, at ANL, to provide
427 direct information about the europium valence state and corroborate any possible changes
428 suggested by the isomer shift measurements. The XAS experiment was carried out at Eu L_3 edge
429 (6.97 keV, $2p_{3/2} \rightarrow 5d$ transition) at pressures up to \sim 36 GPa. A pair of 300 μm culet diamonds
430 were used as anvils. The sintered powder sample (a small piece in \sim 50 μm size) was loaded
431 together with a tiny ruby sphere into the aperture of the laser-drilled beryllium gasket and an
432 insert formed by cubic boron nitride and epoxy. No PTM was added with the sample serving as its
433 own transmission medium. As a result, the PFY-XAS measurements are expected to suffer the
434 most from potentially non-hydrostatic effects. Pressures were measured *in situ* using ruby
435 fluorescence [34]. To avoid heavy absorption by the diamond anvils at these low (\sim 7 keV) x-ray
436 energies, the XAS data were taken with the incident beam going through the beryllium gasket and
437 the absorption signal being taken in fluorescence geometry (90° to the incident beam) using a
438 Pilatus detector. The x-rays were focused to 5 μm (the Full Width Half Maximum (FWHM)). The
439 beam spot location was carefully determined by scanning the sample position to minimize self-
440 absorption.

441 ***Acknowledgments***

442 Work at Ames National Laboratory is supported by the US DOE, Basic Sciences, Material
443 Science and Engineering Division under contract no. DE-AC02-07CH11358. T.J.S. was partially
444 supported by the Center for Advancement of Topological Semimetals (CATS), an Energy Frontier
445 Research Center funded by the U.S. Department of Energy Office of Science, Office of Basic
446 Energy Sciences, through Ames National Laboratory. Work at McGill University is supported by

447 Fonds Québécois de la Recherche sur la Nature et les Technologies, and the Natural Sciences
448 and Engineering Research Council (NSERC) Canada; Work at Argonne National Laboratory is
449 supported by the U.S. Department of Energy, Office of Science, under contract No. DE-AC-02-
450 06CH11357. Portions of this work were performed at GeoSoilEnviroCARS (The University of
451 Chicago, Sector 13), Advanced Photon Source (APS), Argonne National Laboratory. GeoSoilEnviroCARS
452 is supported by the National Science Foundation – Earth Sciences (EAR – 1634415). This research used resources of the Advanced Photon Source, a U.S. Department of
453 Energy (DOE) Office of Science User Facility operated for the DOE Office of Science by Argonne
454 National Laboratory under Contract No. DE-AC02-06CH11357. Use of the COMPRES-
455 GSECARS gas loading system was supported by COMPRES under NSF Cooperative Agreement
456 EAR -1606856 and by GSECARS through NSF grant EAR-1634415 and DOE grant DE-FG02-
457 94ER14466. This research used resources of the Advanced Photon Source, a U.S. Department
458 of Energy (DOE) Office of Science User Facility operated for the DOE Office of Science by
459 Argonne National Laboratory under Contract No. DE-AC02-06CH11357. Portions of this work
460 were performed at HPCAT (Sector 16), APS, ANL. HPCAT operations are supported by DOE-
461 NNSA's Office of Experimental Sciences. GCJ and WB acknowledge the support from the
462 National Science Foundation (NSF) CAREER Award No. DMR-2045760, and the help from Y.
463 Xiao at APS, ANL, to set up the beamline. W. X. and H-Z W are supported by the U. S.
464 Department of Energy (DOE), Office of Science, Basic Energy Sciences under award DE-
465 SC0023648. PCC would like to thank Richard Olson for having helped enable the completion of
466 this work.

468 **References**

- 469 1. C. M. Varma. Mixed-valence compounds, *Rev. Mod. Phys.* 48.2: 219 (1976).
- 470 2. J. Arvanitidis, K. Papagelis, S. Margadonna, K. Prassides, and A. N. Fitch, Temperature-
471 Induced Valence Transition and Associated Lattice Collapse in Samarium Fulleride,
472 *Nature* 425.6958: 599-602 (2003).
- 473 3. M. M. Abd-Elmeguid, Ch. Sauer, and W. Zinn, Pressure-Induced Valence Change of Eu
474 in Eu(Pd_{0.8}Au_{0.2})₂Si₂: Collapse of Magnetic Order, *Phys. Rev. Lett.* 55, 2467(1985).
- 475 4. Y. Matsumoto, S. Nakatsuji, K. Kuga, Y. Karaki, N. Horie, Y. Shimura, T. Sakakibara, A.
476 H. Nevidomskyy, and P. Coleman, Quantum Criticality Without Tuning in the Mixed
477 Valence Compound β -YbAlB₄, *Science* 331, 316 (2011).
- 478 5. M. Okawa, M. Matsunami, K. Ishizaka, R. Eguchi, M. Taguchi, A. Chainani, Y. Takata, M.
479 Yabashi, K. Tamasaku, Y. Nishino *et al.*, Strong Valence Fluctuation in the Quantum
480 Critical Heavy Fermion Superconductor β -YbAlB₄: A Hard X-Ray Photoemission Study,
481 *Phys. Rev. Lett.* 104, 247201 (2010).
- 482 6. M. Dzero, M. R. Norman, I. Paul, C. Pépin, and J. Schmalian, Quantum Critical End Point
483 for the Kondo Volume Collapse Model, *Phys. Rev. Lett.* 97, 185701 (2006).
- 484 7. M. Wakushima, Y. Doi, Y. Hinatsu, and N. Masaki, Mössbauer Effects and Magnetic
485 Properties of Mixed Valent Europium Sulfide, EuPd₃S₄, *J. Solid State Chem.* 157, 117
486 (2001).
- 487 8. P. Bonville, C. Godart, E. Alleno, F. Takahashi, E. Matsuoka, and M. Ishikawa,
488 Heterogeneous mixed valence in YbPd₃S₄: evidence from ¹⁷⁰Yb Mössbauer and x-ray L_{III} -
489 edge absorption measurements, *J. Phys.: Condens. Matter.* 15, L263 (2003).
- 490 9. D. H. Ryan, S. L. Bud'ko, B. Kuthanazhi, and P. C. Canfield, Valence and magnetism in
491 EuPd₃S₄ and (Y,La)_xEu_{1-x}Pd₃S₄, *Phys. Rev. B* 107, 014402 (2023).

492 10. T. Berry, V. C. Morano, T. Halloran, X. Zhang, T. J. Slade, A. Sapkota, S. L. Budko, W.
493 Xie, D. H. Ryan, Z. Xu *et al.*, Formation of a simple cubic antiferromagnet through charge
494 ordering in a double Dirac material, *arXiv:2303.02218* (2023).

495 11. R. Lübbers, G. Wortmann, and H. F. Grünsteudel, High-pressure studies with nuclear
496 scattering of synchrotron radiation, *Hyperfine Interactions* 123/124, 529-559 (1999).

497 12. B. K. Cho, J.-S. Rhyee, J. Y. Kim, M. Emilia, and P. C. Canfield, Anomalous
498 magnetoresistance at low temperatures in a single crystal of GdB_4 , *J. Appl. Phys.* 97,
499 10A923 (2005).

500 13. J. Y. Kim, N. H. Sung, B. Y. Kang, M. S. Kim, B. K. Cho, and J.-S. Rhyee, Magnetic
501 anisotropy and magnon gap state of SmB_4 single crystal, *J. Appl. Phys.* 107, 09E111
502 (2010).

503 14. C. Hermann, Zur systematischen Strukturtheorie. IV. Untergruppen, *Z. Kristallogr.* 69,
504 533 (1929).

505 15. S. Deonarine and J. L. Birman, Group-subgroup phase transitions, Hermann's space-
506 group decomposition theorem, and chain subduction criterion in crystals, *Phys. Rev. B*
507 27, 4263 (1983).

508 16. S. Klotz, J.-C. Chervin, P. Munsch, and G. Le Marchand, Hydrostatic limits of 11 pressure
509 transmitting media, *J. Phys. D: Appl. Phys.* 42 (7), 075413 (2009).

510 17. A. Jayaraman, V. Narayananmurti, E. Bucher, and R. G. Maines, Continuous and
511 discontinuous semiconductor-metal transition in Samarium monochalcogenides under
512 pressure, *Phys. Rev. Lett.* 25, 368 (1970).

513 18. A. I. Goldman, A. Kreyssig, K. Prokeš, D. K. Pratt, D. N. Argyriou, J. W. Lynn, S. Nandi,
514 S. A. J. Kimber, Y. Chen, Y. B. Lee *et al.*, Lattice collapse and quenching of magnetism in
515 CaFe_2As_2 under pressure: A single-crystal neutron and x-ray diffraction investigation,
516 *Phys. Rev. B* 79, 024513 (2009).

517 19. P. C. Canfield, S. L. Bud'ko, N. Ni, A. Kreyssig, A. I. Goldman, R. J. McQueeney, M. S.
518 Torikachvili, D. N. Argyriou, G. Luke, and W. Yu, Structural, magnetic and
519 superconducting phase transitions in CaFe_2As_2 under ambient and applied pressure,
520 *Physica C* 469, 404–412 (2009).

521 20. P. W. Anderson, and S. T. Chui, Anharmonic strain effects in crystals and mixed valence
522 states, *Phys. Rev. B* 9, 8 (1974).

523 21. W. Sturhahn, CONUSS and PHOENIX: Evaluation of nuclear resonant scattering data.
524 *Hyperfine Interact.* 125, 149-172 (2000).

525 22. F. H. Yu, H. M. Mu, W. Z. Zhuo, Z. Y. Wang, Z. F. Wang, J. J. Ying, and X. H. Chen,
526 Elevating the magnetic exchange coupling in the compressed antiferromagnetic axion
527 insulator candidate EuIn_2As_2 , *Phys. Rev. B* 102, 180404(R) (2020).

528 23. L. Zhao, C. Yi, C.-T. Wang, Z. Chi, Y. Yin, X. Ma, J. Dai, P. Yang, B. Yue, J. Cheng *et al.*,
529 Monoclinic EuSn_2As_2 : A novel high-pressure network structure, *Phys. Rev. Lett.* 126,
530 155701 (2021).

531 24. W. Bi, T. Culverhouse, Z. Nix, W. Xie, H.-J. Tien, T.-R. Chang, U. Dutta, J. Zhao, B.
532 Lavina, E. E. Alp *et al.*, Drastic enhancement of magnetic critical temperature and
533 amorphization in topological magnet EuSn_2P_2 under pressure, *npj Quantum Mater.* 7:43
534 (2022).

535 25. R. A. Susilo, W. Deng, J. Feng, A. Wang, N. Kawamura, N. Ishimatsu, S. Kawaguchi, M.
536 Yuan, H. Li, W. Ren *et al.*, Impacts of pressure to the structural, electronic and magnetic
537 properties of Dirac semimetal EuMnBi₂, *Phys. Rev. Research* 3, 043028 (2021).

538 26. Y. Ōnuki, M. Hedo, and F. Honda, Unique Electronic States of Eu-based Compounds, *J.*
539 *Phys. Soc. Jpn.* 89, 102001 (2020).

540 27. C. U. Segre, M. Croft, J. A. Hodges, V. Murgai, L. C. Gupta, and R. D. Parks, Valence
541 Instability in Eu(Pd_{1-x}Au_x)₂Si₂: The Global Phase Diagram, *Phys. Rev. Lett.* 49, 1947
542 (1982).

543 28. T. J. Slade, and P. C. Canfield, Use of Refractory Volatile Element Deep Eutectic
544 Regions to Grow Single Crystalline Intermetallic Compounds, *Z. Anorg. Allg. Chem.* 10.
545 1002 (2022).

546 29. P. C. Canfield, T. Kong, U. S. Kaluarachchi, and N. H. Jo, Use of frit-disc crucibles for
547 routine and exploratory solution growth of single crystalline samples, *Philos. Mag.* 96:1,
548 84–92 (2016).

549 30. Canfield Crucible Sets, <https://www.lspceramics.com/canfield-crucible-sets-2>.

550 31. Bjscistar, http://www.bjscistar.com/page169?product_id=127.

551 32. A. Celeste, F. Borondics, and F. Capitani, Hydrostaticity of pressure-transmitting media
552 for high pressure infrared spectroscopy, *High Pressure Res.* 39 (4), 608–618 (2019).

553 33. D. D. Ragan, D. R Clarke, and D. Schiferl, Silicone fluid as a high-pressure medium in
554 diamond anvil cells. *Rev. Sci. Instrum.* 67 (2), 494–496 (1996).

555 34. G. Shen, Y. Wang, A. Dewaele, C. Wu, D. E. Fratanduono, J. Eggert, S. Klotz, K. F.
556 Dziubek, P. Loubeyre, O. V. Fat'yanov *et al.*, Toward an international practical pressure
557 scale: A proposal for an IPPS ruby gauge (IPPS-Ruby2020), *High Press. Res.* 40, 299–
558 314 (2020).

559 35. C. Prescher, and V. B. Prakapenka, DIOPTAS: a program for reduction of two-
560 dimensional x-ray diffraction data and data exploration, *High. Press. Res.* 35, 223–230
561 (2015).

562 36. B. H. Toby, and R. B. Von Dreele, GSAS-II: the genesis of a modern open-source all-
563 purpose crystallography software package, *J. Appl. Crystallogr.* 46, 544–549 (2013).

564 37. J. Y. Zhao, W. Bi, S. Sinogeikin, M. Y. Hu, E. E. Alp, X. C. Wang, C. Q. Jin, and J. F. Lin,
565 A compact membrane-driven diamond anvil cell and cryostat system for nuclear resonant
566 scattering at high pressure and low temperature, *Rev. Sci. Instrum.* 88, 125109 (2017).

567 38. G. Wortmann, U. Ponkratz, Bi. Bielemeier, and K. Rupprecht, Phonon density-of-states in
568 bcc and hcp Eu metal under high pressure measured by ¹⁵¹Eu nuclear inelastic scattering
569 of synchrotron radiation, *High. Press. Res.* 28, 545–551 (2008).

570 39. N. M. Souza-Neto, J. Zhao, E. E. Alp, G. Shen, S. V. Sinogeikin, G. Lapertot, and D.
571 Haskel, Reentrant valence transition in EuO at high pressures: beyond the bond-valence
572 model, *Phys. Rev. Lett.* 109, 026403 (2012).

573 40. W. Bi, Z. Nix, U. Dutta, J. Zhao, E. E. Alp, D. Zhang, P. Chow, Y. Xiao, Y.-B. Liu, G.-H.
574 Cao, and Y. K. Vohra, Microscopic phase diagram of Eu(Fe_{1-x}Ni_x)As₂ (x = 0, 0.04) under
575 pressure, *Phys. Rev. B* 103, 195135 (2021).

577

578

579

580

581

Figures and Tables

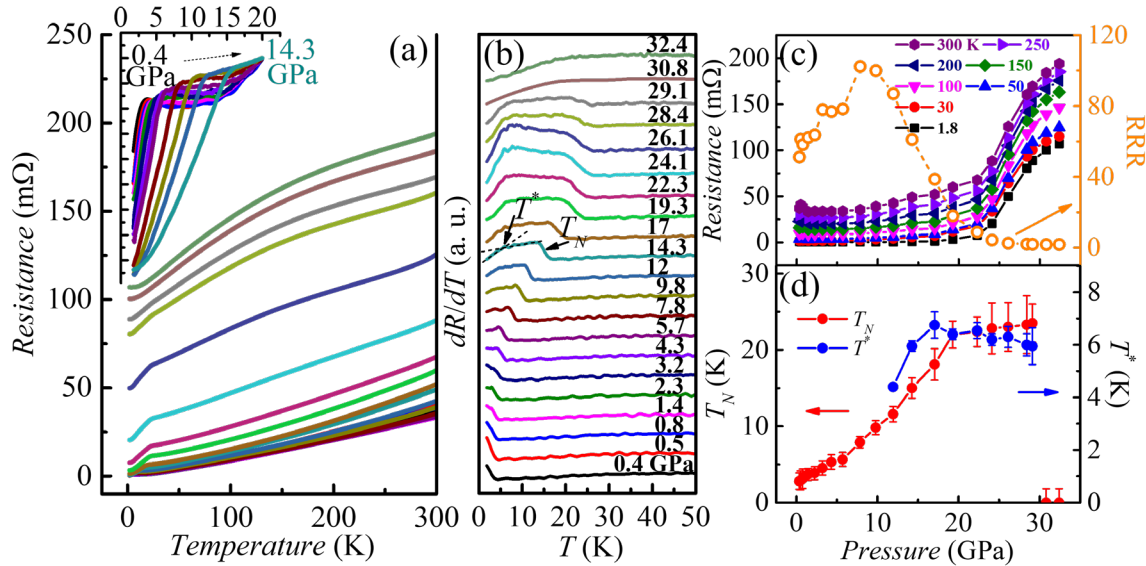


Fig. 1. Pressure dependence of electrical resistance and T_N . Temperature dependencies of the (a) electrical resistance and (b) temperature derivatives of the resistance for single crystal EuPd_3S_4 , measured at different pressures. (a) and (b) share the same legend. The inset in (a) shows the zoomed-in resistance curves normalized at 20 K from 0.4 GPa to 14.3 GPa so as to better show the evolution of T_N below 14.3 GPa. In (b), curves at various pressures are offset from each other so as to better show the evolution of T_N . T_N is determined as the midpoint of the dR/dT shoulder, and T^* is defined as the intersection of two black dashed lines drawn from high temperature and low temperature. (c) Resistance at various temperatures and the residual resistivity ratio (RRR) as functions of pressure. (d) T_N and T^* as functions of pressure.

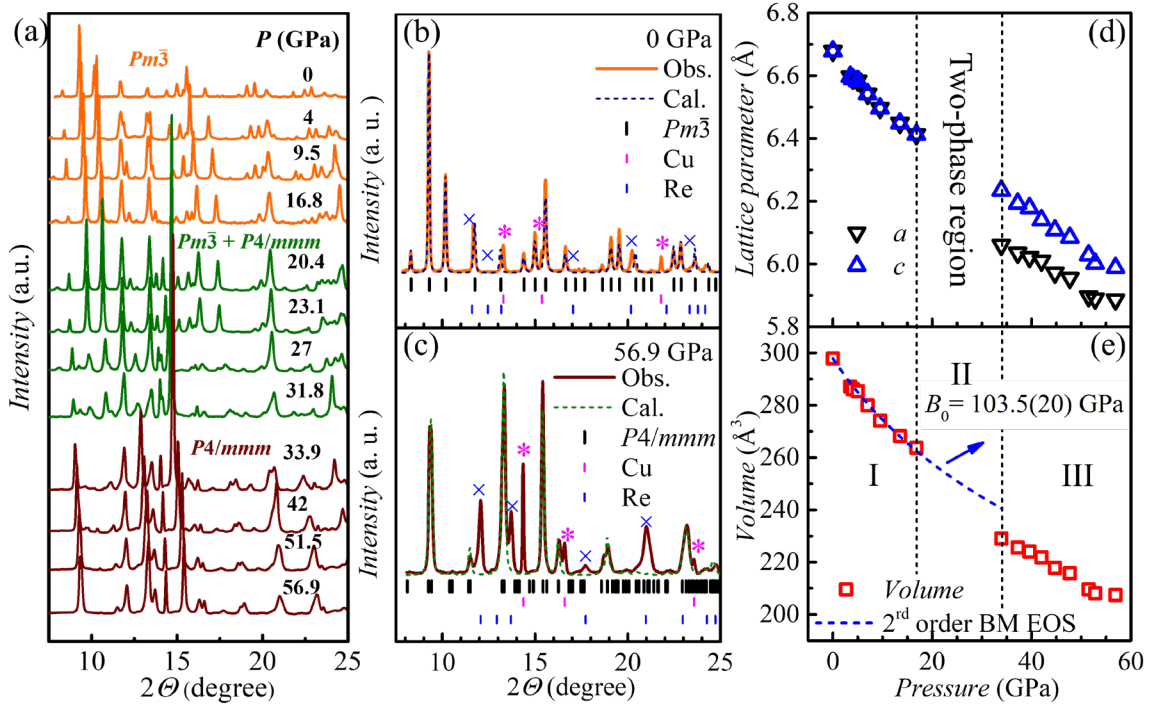


Fig. 2. Pressure induced structural phase transition. (a) Selective powder x-ray diffraction (PXRD) patterns of EuPd₃S₄ at various pressures from 0 GPa to 56.9 GPa. The synchrotron x-ray wavelength λ is 0.4833 Å. The data was collected at room temperature. The full set is shown in Fig. S1. (b) Rietveld refinement of the PXRD pattern at ambient pressure. (c) Le Bail fit to the high-pressure P4 / mmm structure at 56.9 GPa. The pink stars and blue crosses in (b) and (c) represent the clear extra peaks in the PXRD spectra of copper (pressure manometer) and rhenium (gasket), respectively. (d) Pressure dependences of the refined lattice constants a, and c. (e) Pressure dependence of the unit cell volume. The blue dashed curve shows the fitting by second-order Birch-Murnaghan equation of state (BM EOS). Several sets of independent PXRD measurements in zone I have been performed and show the same evolution of volume with the pressure. A more detailed plot is shown in Fig. S5.

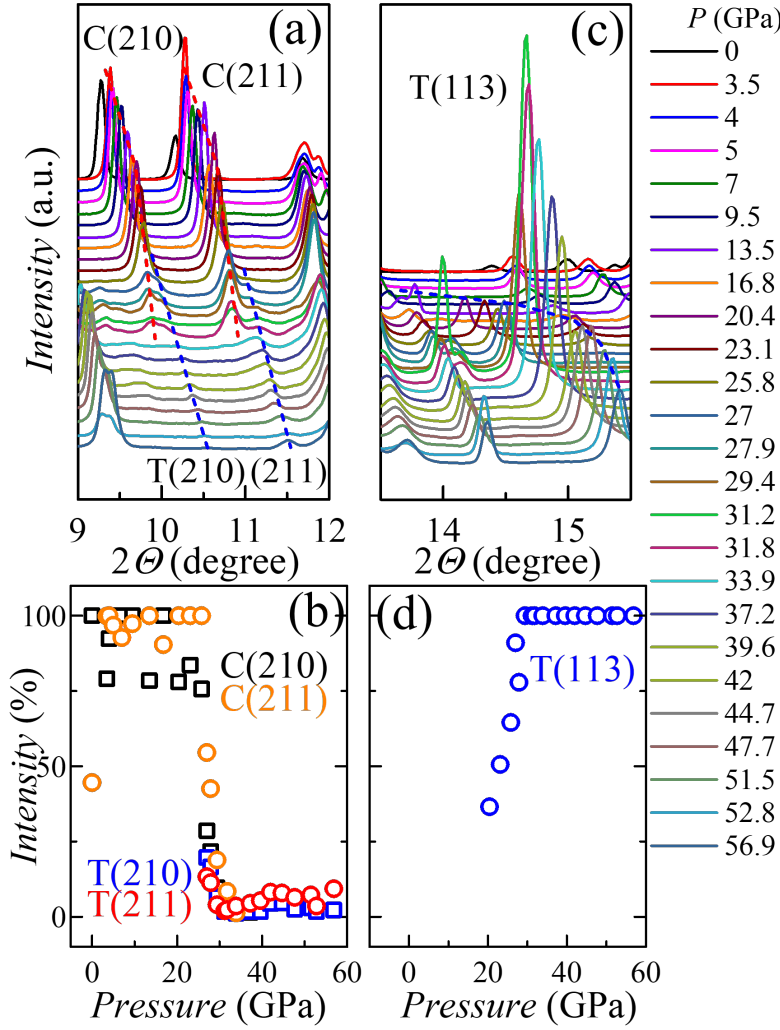


Fig. 3. The evolution of diffraction peaks with the pressure in selected 2θ ranges. (a), (b) the cubic phase (210) and (211) (“cubic” is identified by “C”) to tetragonal (210) and (211) (“tetragonal” is identified by “T”); (c), (d) the emergence of T(113). (a) and (c) share the same legend. The red and blue dashed curves in (a) and (c) are the smooth guides to the eye of the position change of diffraction peaks. The percentage of the intensities in (b) and (d) are estimated by: (intensity of peak)/ (maximum peak intensity in the spectrum).

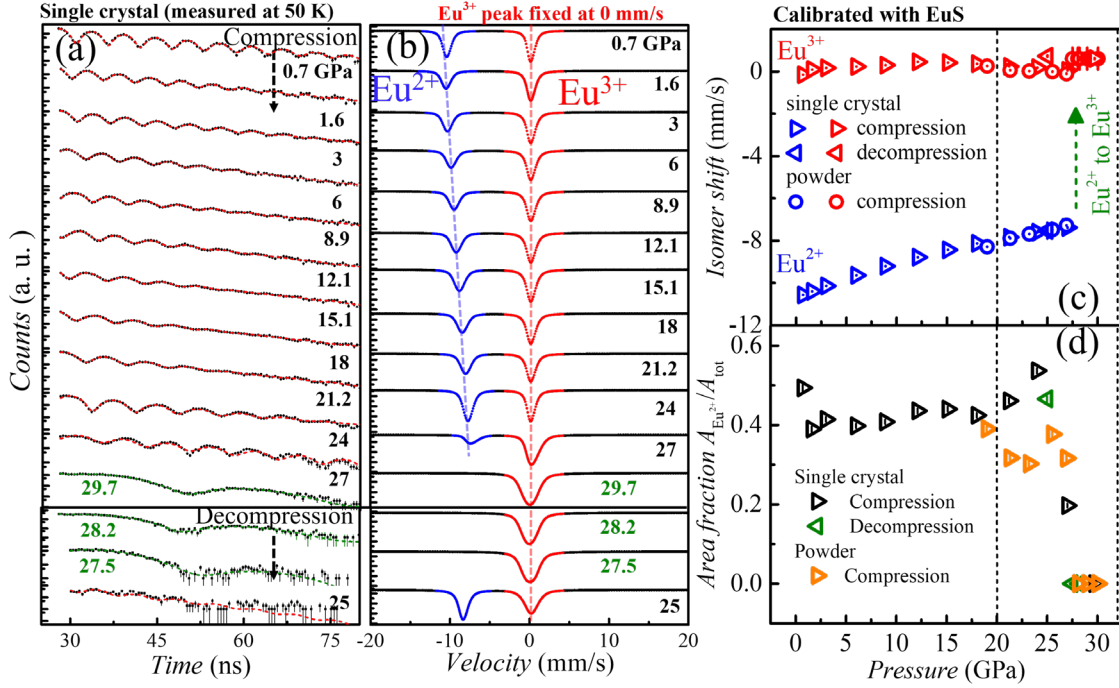


Fig. 4. Pressure-induced Eu valence transition from the isomer shift measurements. (a) The time domain ^{151}Eu Synchrotron Mössbauer spectroscopy spectra (SMS) of EuPd_3S_4 at 50 K under various pressures taken using a single crystal sample with helium as the pressure transmitting medium. The pressure was measured at 50 K. Pressure was first increased from 0.7 GPa to 29.7 GPa, then decreased to 25 GPa, in order to assess the reversibility of the pressure and the valence transition. The red dotted curves are fit to the SMS spectra using CONUSS [21]. (b) Simulated energy-domain Mössbauer spectra based on the fitting results from each corresponding SMS spectrum. For these simulated patterns, the isomer shift of the Eu^{3+} peak was fixed to zero and only changes in the isomer shift and weight of the Eu^{2+} peaks are apparent. In (b), the blue and red dashed lines serve as visual aids to illustrate the evolution of Eu^{2+} isomer shift while Eu^{3+} remains fixed. The calibrated (using the EuS standard) pressure dependence of the absolute isomer shifts for the Eu^{2+} and Eu^{3+} peaks are shown for both samples in (c), while (d) shows the pressure dependence of the Eu^{2+} area fraction. The absolute value of isomer shift is calibrated by moving a reference sample (EuS, at room temperature and ambient pressure, with known isomer shift of Eu^{2+} at -11.496 mm/s) on the beam line. The detailed calibration process is explained in Fig. S8, S9.

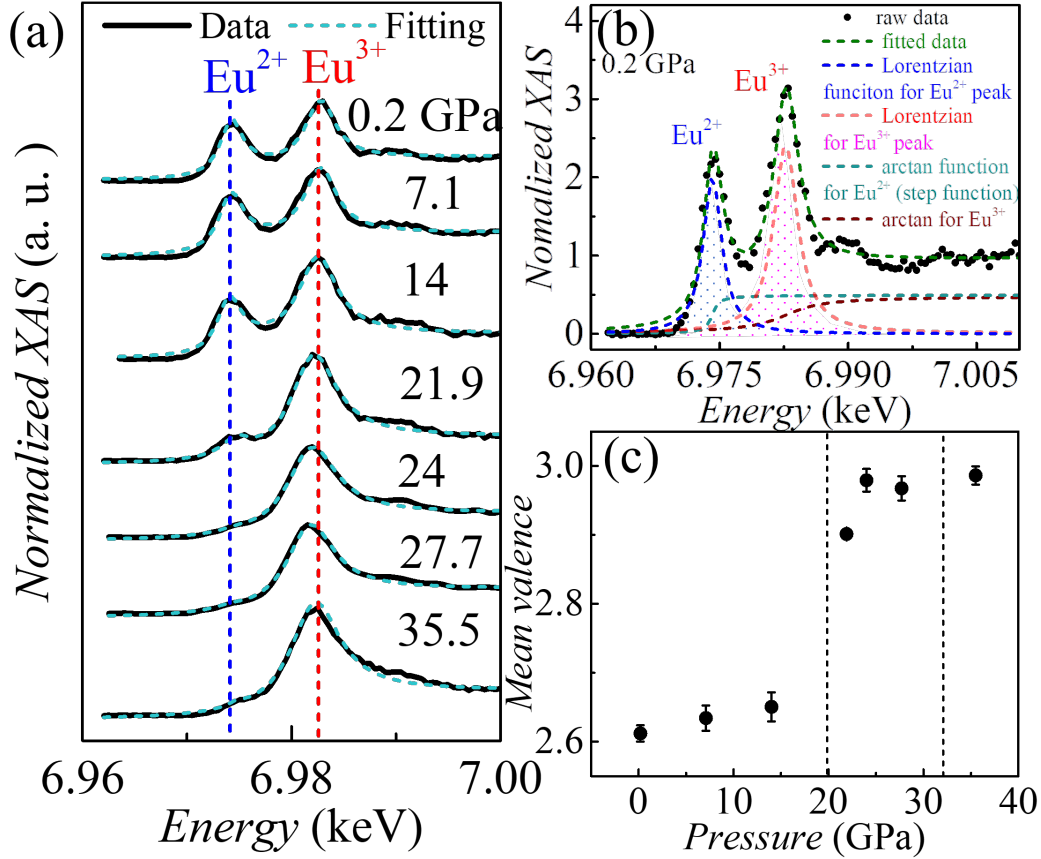


Fig. 5. Pressure induced valence transition from absorption spectra. (a) partial fluorescence-yield x-ray absorption spectroscopy (PFY-XAS) data at Eu L_3 absorption edge in EuPd₃S₄ at room temperature at pressures from 0.2 GPa to 35.5 GPa showing the valence transition from roughly 50:50 Eu²⁺:Eu³⁺ to essentially Eu³⁺. The blue and red vertical dashed lines are guides to the eye showing the absorption peak energies for Eu²⁺ and Eu³⁺, respectively. (b) Fits to the 0.2 GPa PFY-XAS data (described in the text). The red dashed line represents the total summation of 2 arctangent step functions and 2 Lorentzian peaks. (c) Mean Eu valence as a function of the pressure. The mean valence is estimated by from the ratio of the areas of fitted Lorentzian peaks.

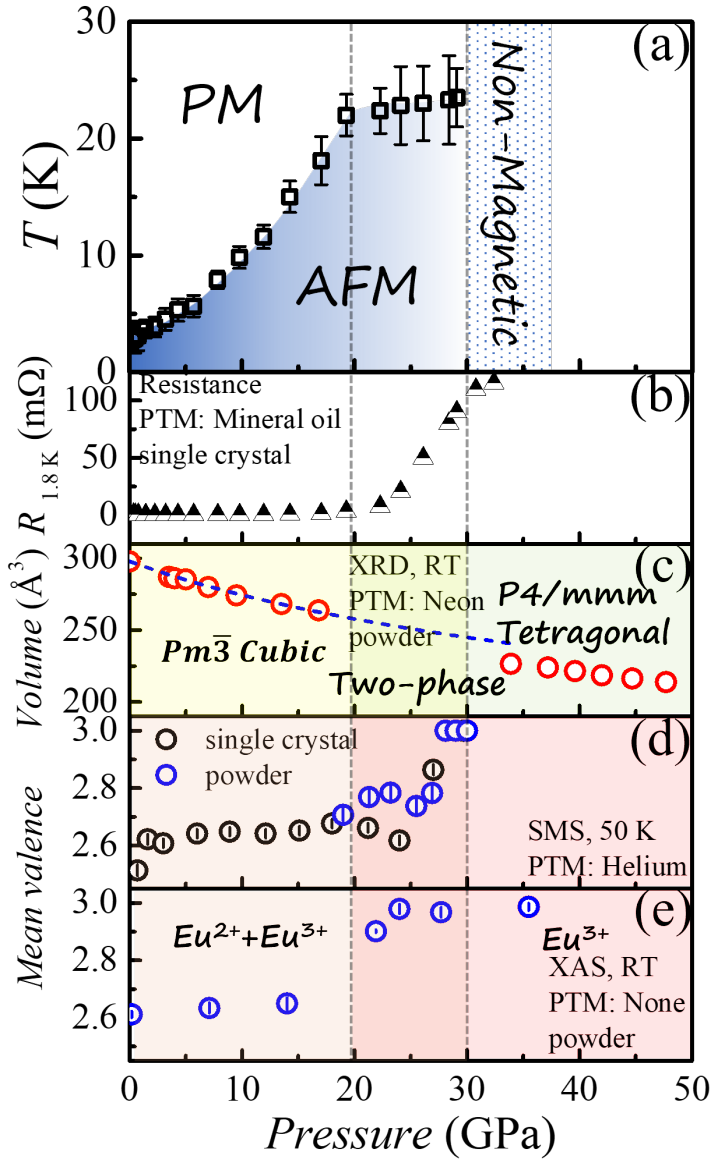


Fig. 6. Pressure dependence of electronic, magnetic, and structural properties of EuPd_3S_4 .

The pressure dependence of (a) AFM transition temperature T_N , (b) resistance at 1.8 K, (c) unit cell volume estimated from the high-pressure x-ray diffraction measurement, (d) mean valence estimated from the Synchrotron Mössbauer spectroscopy (SMS) spectra, and (e) mean valence estimated from the Partial fluorescence-yield x-ray absorption spectroscopy (PFY-XAS) spectra. PTM: pressure transmitting medium. RT: room temperature. The blue dashed curve in (c) is the second-order BM EOS fitted curve that shows the clear difference in the unit cell volume between zone I and zone III. The vertical dashed lines crossing all panels mark the lower and upper boundaries of the two-phase region determined from x-ray diffraction.